# Accepted Manuscript


Structural and optical properties of ZnO and manganese-doped ZnO

María V. Gallegos, Miguel A. Peluso, Horacio Thomas, Laura C. Damonte, Jorge E. Sambeth

PII: S0925-8388(16)32319-2

DOI: 10.1016/j.jallcom.2016.07.283

Reference: JALCOM 38452

To appear in: *Journal of Alloys and Compounds*

Received Date: 15 June 2016

Revised Date: 23 July 2016

Accepted Date: 26 July 2016

Please cite this article as: M.V. Gallegos, M.A. Peluso, H. Thomas, L.C. Damonte, J.E. Sambeth, Structural and optical properties of ZnO and manganese-doped ZnO, *Journal of Alloys and Compounds* (2016), doi: 10.1016/j.jallcom.2016.07.283.

# Structural and optical properties of ZnO and Manganese-doped ZnO

**María V. Gallegos[a], Miguel A. Peluso[a], Horacio Thomas[a,b], Laura C. Damonte[c*] and Jorge E. Sambeth[a*]**

[a]*Centro de Investigación y Desarrollo en Ciencias Aplicadas "Dr. Jorge J. Ronco" (CINDECA, CONICET-FCE UNLP), 47 Nro 257, La Plata, Buenos Aires(Argentina)*

[b]*PlantaPilotoMultipropósito, (PlaPiMu, CICPBA-UNLP) Av. Cno. Centenario y 506, M. B. Gonnet, Buenos Aires (Argentina)*

[c]*Instituto de Física La Plata – (IFLP, CONICET – FCE UNLP) calle 49 y 115, La Plata, Buenos Aires (Argentina)*

*Corresponding author.

*E-mail address: damonte@fisica.unlp.edu.ar sambeth@quimica.unlp.edu.ar*

Keywords: Mn - ZnO, structural properties, optical properties, XPS, band gap energy.

**ABSTRACT**

The structural, morphological and optical properties of manganese oxides supported on commercial ZnO, prepared by impregnation with manganese nitrate, were investigated. The nominal compositions of Mn in the samples were 5, 10, 15 and 20 %w/w.The X-ray diffraction (XRD) experiments revealed the presence of the ZnO wurtzite phase in all the samples, and $ZnMnO_3$ was also found in the samples with 15 wt% and 20 wt% of Mn. X-ray photoelectron spectroscopy (XPS) showed the presence of $Mn^{2+}$ and $Mn^{4+}$ in the xMnZnO samples. The results showed that the $Mn^{2+}$ ions had

substituted the $Zn^{2+}$ ions without changing the wurtzite structure of ZnO, while $Mn^{4+}$ might be assigned to the $ZnMnO_3$ impurity phase. The optical band gap was found to be 3.3 eV for undoped ZnO samples and 3.10 eV for Mn-doped samples. The lattice defect distribution was investigated using the positron annihilation method. The results revealed that the average lifetime is a function of the Mn concentration and the formation of the $ZnMnO_3$ phase.

## 1. Introduction

ZnO is one of the most important metal oxides due to its unique physical characteristics of wide and direct band gap (3.37 eV at room temperature). It is used in various applications such as optoelectronics [1–4], sensors [3–7] pharmaceuticals, etc. Additionally, ZnO is used as photocatalyst [5,6] and in different catalytic reaction such as steam reforming of alcohols [7,8], synthesis of methanol [9] and complete oxidation of CO [10] and trichloroethylene [11]. Also, doping ZnO with transition metal such as Mn and Cu could affect the electronic surface band structure of ZnO and change its applications [10,12,13].

For synthesis of Mn doped ZnO bulk particles, several techniques such as reverse micelle [14], solid state reaction [15], sol-gel [16], solvothermal [17] and co-precipitation [18] have been employed. Compare to others, impregnation has some advantages, for instance; easy synthesis, reproducibility, low temperature and inexpensive.

Naturally, the interaction of doped atoms with the defects will modify the properties of the material in different ways, depending on the nature and concentration of the doped atoms. Positron annihilation spectroscopy (PALS) has been used to characterize surface defects in nanoparticles, due to its extreme sensitivity to the presence of vacancies in the

material [19]. Positron annihilation spectroscopy has been used to study different metal doped ZnO particles usually prepared by solid state reaction of ZnO and a metal oxide [20], such as $Fe_2O_3$ [21] and $MnO_2$ [22–24]. Chemical reaction forces the dopant element to be introduced into the crystal structure of the compound.

The aim of this paper is to evaluate and discuss the effect of Mn doping on the ZnO structure and its optoelectronic properties. The solids were prepared by impregnation of ZnO with $Mn(NO_3)_2.4H_2O$, and the samples were characterized by a variety of techniques including X-ray diffraction, scanning electronmicroscopy, UV-Vis, and positron annihilation lifetime spectroscopy (PALS).

## 2. Experimental

### *2.1. Sample preparation.*

Commercial ZnO (99.99%, Alfa Aesar, Johnson Matthey Co.) was previously calcined in air at 500 ºC during 2 hs.

The Mn-doped ZnO samples with nominal compositions (wt% = 5, 10, 15 and 20) of Mn were synthesized by the wet impregnation method. In a typical procedure, 5 g of commercial ZnO was added to 50 mL of $Mn(NO_3)_2.4H_2O$ solution with the appropriate concentration, and the suspension was stirred at 30 $^oC$ for 1 h. The products were filtered, washed with distilled water, and dried at 120 $^oC$ for 24 h. Finally, the solids were calcined in air at 500 $^oC$ for 2 h. The samples were named xMnZnO, where x is the nominal Mn wt% concentration of the sample. The nomenclature of the samples is listed in Table 1.

The obtained powders were pressed into 8 mm diameter pellets for positron annihilation lifetime measurements.

*2.3. Characterization*

The manganese content was measured in a Varian AA 240 spectrophotometer after dissolving the catalysts in aqua regia.

The samples were characterized by X-ray diffraction (XRD) methods using a Philips diffractometer. The diffraction patterns were recorded at room temperature from 15 to 80º of 2θ using Cu $K_\alpha$ ($\lambda$ = 1.5406 Å) radiation at 0.02º $min^{-1}$ scanning speed and a counting time of 2 s per step.

The BET specific areas were measured by $N_2$ adsorption at liquid nitrogen temperature (77 K) in a Micromeritics Accusorb 2100 D sorptometer.

The surface morphology of the samples was studied using scanning electron microscopy (SEM) in a Philips SEM 505 microscope.

TEM measurements were performed with a JEOL 100 CXII microscope operated at 100 kV.

X-ray photoelectron spectra (XPS) of the samples were obtained using a multitechnique system, with a Mg X-ray source and a hemispherical PHOIBOS 150 analyzer operating in the fixed analyzer transmission mode. Binding energies (BE: ±0.1 eV) were calculated using adventitious hydrocarbon (C 1s = 284.6 eV) as the internal reference. Curve fitting was performed with the CasaXPS software.

Optical characterizations were carried out by measuring the diffuse reflectance spectroscopy. All spectra were taken in the range of 200 - 800 nm using Perkin Elmer Lamdba 35 UV-vis spectrophotometer with integrating sphere attachment and spectralon reflectance standard.

Positron annihilation lifetime measurements were collected in a conventional fast–fast coincidence system with two scintillator detectors (one $BaF_2$ and one plastic BURLE), which provided a time resolution (FWHM) of 260 ps. The radioactive source, $^{22}NaCl$ (10 μCi), was deposited onto a Kapton foil (1.42 g $cm^{-3}$) and sandwiched between two sample specimens. The source contribution (386 ps of 15% intensity assigned to the Kapton foil and a second one of around 1 ns with less than 1% intensity due to annihilation in the surroundings of the source) and the response function were evaluated from a reference sample (Hf metal) using the RESOLUTION code [25]. The lifetime spectra (2–3x$10^6$ counts) were acquired at room temperature and analyzed with the POSITRONFIT program [25].

## 3. Results

### *3.1. Catalysts Characterization*

The nomenclature, along with the manganese content and the specific area of the studied samples, is listed in Table 1. The sample specific surface area gradually increases with the increase in manganese content.

A similar behavior was also observed when $TiO_2$ is impregnated with $Mn(NO_3)_2$ precursor [26], and in several Mn-doped ZnO samples prepared by different routes [5,27,28]. Also, Bhattacharyya and Gedanken [29] found that the surface area of Ag/ZnO composites increases due to the formation of Ag cluster over ZnO. In our work, the increment in surface area could be associated to the formation of a segregated $ZnMnO_3$ phase, or by the decreasing grain size [30].

XRD patterns of the samples are shown in Fig. 1. The diffraction peaks of the undoped ZnO can be identified as belonging to a ZnO phase with a hexagonal wurtzite crystal structure [JCPDF card 36-1451] in which the strong diffraction peaks appear in (1 0 0),

(0 0 2) and (1 0 1) respectively [31]. Mn-doped ZnO samples also present the peaks corresponding to hexagonal wurtzite. However, in samples 15MnZnO and 20MnZnO, the appearance of additional peaks at $2\theta = 30$ and 35.5º, matches well with diffraction patterns of face-centered cubic $ZnMnO_3$ [JCPDF 19-1461]. This last compound has been detected by other authors as an impurity phase. Its structure has not been clearly reported, however recent works have demonstrated that the $ZnMnO_3$ phase has a related-spinel structure [32,33]. Mn has a solid solubility limit of about 13% in ZnO matrix [34]. The Mn concentration in the samples 15MnZnO and 20MnZnO are beyond the solid solubility limit, which could be responsible for the presence of $ZnMnO_3$ secondary phase. On the contrary, the Mn concentration of the samples 5MnZnO and 10MnZnO are smaller than the solid solubility limit and the Mn ions were possibly diluted in the ZnO host matrix.

Nevertheless, the existence of secondary phases in samples 5MnZnO, 10MnZnO cannot be excluded. Some secondary phases may be too small to be detected by XRD analysis and microstructures could not be seeing by TEM [34,35].

As the Mn content increases, the diffraction intensity from ZnO (1 0 1) peaks drops, possibly due to a decrease in the crystallite size and crystalline quality [27]. In addition, a shift of (1 0 1) peak positions was observed. This is probably due to the substitution of the relatively large ionic radius $Mn^{2+}$ (0.080 nm) ions at the smaller radius $Zn^{2+}$ (0.074 nm) sites [24,36,37]. On the other hand, the formation of $ZnMnO_3$ is attributed to the much smaller radius of $Mn^{4+}$ (0.060 nm) than that of $Zn^{2+}$.

The average crystal size (D) of the ZnO and Mn doped ZnO samples, was estimated using the Scherrer formula:

$$D = \frac{0.9\,\lambda}{\beta \cos\theta}$$

where λ is the X-ray wavelength, β is the angular line width of half maximum intensity, and θ is Bragg's diffraction angle. Results are shown in Table 2. The crystallite size (D) in general has no change, except for the sample 20MnZnO. D has a little increment when manganese concentration reaches 5%, and then decrease when more manganese is added [38]. It means that some Mn ions may remain adhered to ZnO surface and not associated with ZnO lattice [39]. When the manganese concentration reaches near 20%, the decreases in the D value is more notorious, in coincident with other authors [40, 41].

The influence of different percentages of Mn on the surface morphologies of commercial ZnO was studied by SEM (figure not show). With the increase in the manganese amount, higher agglomeration is observed. Fig. 2 (a) and (b) shows the SEM image of ZnO and 10MnZnO samples, respectively. Manganese addition to ZnO generates irregular globular particles. Fig. 2 (c) shows the TEM image of 10MnZnO sample. Different kinds of shape, such as irregularly shaped nanoparticles, larger rectangular platelets and hexagonally shaped nanoparticles, are visible in the 10MnZnO sample.

In order to know about the chemical bonding structure of Mn-doped ZnO samples, the XPS spectra for the valence bonds of Mn $2p_{3/2}$, Zn $2p_{3/2}$ and O 1s states were recorded. The corresponding binding energies of the above states are summarized in Table 3. As shown in Fig. 3, the spectra of Zn $2p_{3/2}$ of the ZnO and Mn-doped ZnO samples exhibit a symmetric single peak that could be nicely fitted to a single peak, ruling out the possibility of existence of a multiple component of Zn in these samples.

The peak corresponding to $Zn^{2+}$ ions in ZnO, shifted to lower binding energies as a function of the Mn concentration (see Table 3). This shift in binding energy is due to the partial substitution of Zn in ZnO lattice by $Mn^{2+}$ ions and Zn–Mn bonding structure [42]. In addition, as it was remarked by Ilyas et al., [43] the different bonding states of

the elements on the surface will result in a shift in the binding energy towards a lower value. Zn atoms bonded to manganese (which are less electronegative than oxygen) will contribute to the shift of the Zn $2p_{3/2}$ peak [44]. Another reason of the shift in the binding energy could be the reduced average crystallite size, which is coincident with the XRD results [45].

The O1s spectra of the samples are plotted in Fig. 4. In the Mn-doped ZnO samples the O 1s peak could be reproduced by two components: a low binding energy peak (OI), ascribed to lattice O and a high binding energy peak (OII), assigned to surface adsorbed O, $OH^-$ groups and O vacancies [46]. Some authors have reported a correlation between the surface concentration of the OII species and the catalytic activity, due to the higher mobility of the OII species compared to the OI species [47]. The concentration of OI and OII species are listed in Table 3. The pure ZnO presents higher concentrations of OII species than OI species. When manganese is added to ZnO, in samples 5MnZnO and 10MnZnO, the OII/OI ratio change and reaches the 15 and 28%, respectively. However, when the manganese solubility limit is surpassed (15MnZnO and 20MnZnO), the percentage of OII species is much higher than OI species, suggesting the possibility of the formation of too many oxygen defects in the oxide after the incorporation of manganese in excess [48].

For the evaluation of the Mn valence state, the $Mn2p_{3/2}$ spectra were studied. Although Mn 3s level is usually used for the determination of the Mn oxidation state, this energy region was overshadowed by the presence of a very strong Zn 3p peak, and thus Mn 2p lines were analyzed. The spectra of Mn $2p_{3/2}$ of the manganese supported samples are presented in Fig. 5. In the manganese doped ZnO samples, the Mn2p spectral shape could be related with two $Mn2p_{3/2}$ components centered near 642 eV, which could be associated to $Mn^{2+}$ and $Mn^{4+}$ species [49]. The presence of $Mn^{2+}$ is expected in Mn-

doped ZnO due to the replacement of $Zn^{2+}$ at the lattice site, while $Mn^{4+}$ might be assigned to the $ZnMnO_3$ impurity phase [50]. The area of the two different valence bonds was calculated in order to estimate the atomic concentration of $Mn^{2+}$ and $Mn^{4+}$.

As it can be seen in Table 3, the $Mn^{2+}$ atomic percentage decreases with increasing the manganese content, whereas the $Mn^{4+}$ concentration increases with increasing the manganese content. Similar results were obtained by Duan et al. [50] and Singhal et al. [51] over Mn-doped ZnO nanoparticles.

As the concentration of $Mn^{4+}$ ions increases, the percent of OII species also increases. The presence of the $Mn^{4+}$ ions causes more oxygen vacancies in the surface region of Mn-doped ZnO samples.

The absorption spectra for the manganese-doped ZnO nanoparticles are shown in Fig.6. We plotted the Mn rich samples in Fig. 6(a) and the Mn poor ones in Fig.6 (b) for clarity. There is a drastic change between them; when Mn concentrations reach the solubility limit in ZnO, two different slopes are observed (arrows in Fig. 6(b)).

This phenomenon can be attributed to the formation of a new phase, $ZnMnO_3$, as was also reported by XRD results.

According to Tauc−Mott's relation for allowed direct transitions, the photon energy ($E_f$) dependence of the absorption coefficient ($\alpha$) can be described by [50]:

$$(\alpha E_f)^2 = B(E_f - E_G) \qquad (2)$$

where B is a constant and $E_G$ is the band gap of the material. From Eq. 2, by extrapolating the linear portions to the x-axis and from the corresponding intercepts, the direct energy band gap can be obtained (Fig. 7).

Table 1 lists the obtained values for the band gap energy [eV] as a function of Mn concentration, as well as the values for different Mn oxides taken from the literature. As can be seen, the results demonstrated that Egap changes with Mn concentration [52].

In order to characterize the defects induced by the preparation method, positron annihilation lifetime measurements were performed. The lifetime spectra for all samples were decomposed into three exponential decays according to:

$$n(t) = \sum_i I_i \exp(-t/\tau_i)$$

being the relative intensities $I_i$, normalized, $\Sigma I_i = 1$. After background subtraction and convolution with the resolution function, the parameters that characterized each positron state, $\lambda_i$, annihilation rate ($\lambda_i = 1/\tau_i$) and its intensity $I_i$ are obtained by means of POSITRONFIT program [25].

The presence of two lifetime components is an usual feature for II-VI semiconductor compounds, since intrinsic and extrinsic defects (such as vacancies, interstitials, etc.) introduced during crystal growth and doping are unavoidable [54]. The two-state trapping model [55] predicts a two-component fitting of the spectrum, the shorter one ($\tau_1$) from free annihilation of positrons and the other ($\tau_2$) from trapped positrons at defects. The longest component,$\tau_3$, takes into account the ortho-positronium annihilation formed in large voids present in the material. In the present study, this component (~ 1500ps) maintains its intensity around 3-4% so that has not been included in the forthcoming discussion.

The evolution of positron annihilation parameters with Mn concentration was analyzed. (Fig. 7). The obtained value of $\tau_1$ for the un-doped ZnO (186 ps) is greater than reported values for bulk lifetime but lower than mono-vacancy type defects lifetime for this semiconductor [56]. So the observed first component can be assumed to be a mixed state of positrons annihilating with free electrons in defect-free regions and at structural defects as $V_{Zn}$. As already mention, the second lifetime (~380 ps) is sensing positrons trapped at vacancy clusters (nanovoids) or at intersection interfaces (i.e. triple lines) [56,

57]. No high variation is observed in both lifetime components when Mn atoms are added up to a concentration of 5 wt% (5MnZnO sample) from which a slightly increase is observed in both $\tau_1$ and $\tau_2$. On the contrary, their respectively intensities show a different behavior. While $I_1$ maintains almost constant, $I_2$ increases for 1MnZnO and 5MnZnO indicating an increment in those trapping centers associated to larger open volume defects. For higher Mn contents increase both lifetimes and $I_2$ which may be due to the formation of a new phase with different positron trapping centers.

Since the above-mentioned point defects constitute positron trapping centers leading to similar positron lifetime components that cannot be separated, we also evaluated the average positron lifetime defined by

$$\tau_{ave} = \sum_i I_i \tau_i$$

This statistical parameter displays positron trap behavior independently of the lifetime components proposed for each spectrum. It can be seen from Fig.7 that the average lifetime does not show a monotonic trend with increasing Mn content. This indicates that new positron traps are being generated with doping. The average lifetime decreases from 345 ps for pure ZnO to 323 ps for doped 5MnZnO, showing an increase from this concentration up to 348ps for the highest doped sample 20MnZnO. It is known that ZnO semiconductors present monovacancies in both sublattices, $V_{Zn}$ and $V_O$, the last one being positively charged and unattractive to positrons. Also, the association of different monovacancies can occur, such as divacancies ($V_{Zn}$-$V_O$) or trivacancies ($V_{Zn}$-$V_O$-$V_{Zn}$) [58]. So, the pure ZnO sample has intrinsic point defects yielding a high value for the average lifetime, which is even higher than the known value for single crystals and powders due to its nanosized nature [55]. As doping increased, $Mn^{2+}$ atoms occupied the $V_{Zn}$, reducing the lifetime associated with defects, $\tau_2$, and in consequence,

the average lifetime. This situation remains until the Mn concentration exceeds its solubility limit in ZnO; thereafter, the average lifetime rises/increases again. This fact is in agreement with the above XRD and XPS results, which showed the formation of an impurity phase ($ZnMnO_3$) and the increase of oxygen vacancies (OII species). At this stage, positrons sense many electron densities inside the sample, i.e., two ZnO and $ZnMnO_3$ phases and their corresponding point defects (monovacancies, interstitials, etc.), all of them with similar lifetime values. In consequence, an increment of the average lifetime value is observed.

## Conclusions

A series of manganese oxides supported on commercial ZnO were prepared. XRD data showed that all the samples present the wurtzite structure. An impurity phase ($ZnMnO_3$) was detected in samples 15MnZnO and 20MnZnO. The XPS experiment confirmed the existence of $Mn^{2+}$ and $Mn^{4+}$ species and the increase of oxygen vacancies in the Mn-doped ZnO samples. The results showed that the $Mn^{2+}$ atoms occupied the $V_{Zn}$, reducing the lifetime associated with defects, $\tau_2$, and the average lifetime. This situation remains until the Mn concentration exceeds its solubility limit in ZnO, associated with the formation of $ZnMnO_3$; thereafter, the average lifetime rises again.

**Acknowledgements**

The authors acknowledge the CONICET and UNLP (Argentina). We are thankful to Lic. P. Fetsis and Lic. M. Theiller. This work was supported by CONICET (PIP 942), CICPBA and ANPCyT (PICT 2012-2366).

## References

[1] N. Kiomarsipour, R. Shoja Razavi, Characterization and optical property of ZnO nano-, submicro- and microrods synthesized by hydrothermal method on a large-

scale, Superlattices Microstruct. 52 (2012) 704–710.

[2] S. Benramache, B. Benhaoua, Influence of substrate temperature and Cobalt concentration on structural and optical properties of ZnO thin films prepared by Ultrasonic spray technique, Superlattices Microstruct. 52 (2012) 807–815.

[3] T.T. Trinh, N.H. Tu, H.H. Le, K.Y. Ryu, K.B. Le, K. Pillai, J. Yi, Improving the ethanol sensing of ZnO nano-particle thin films - The correlation between the grain size and the sensing mechanism, Sensors Actuators, B Chem. 152 (2011) 73–81.

[4] Y. Sun, Z. Zhao, P. Li, G. Li, Y. Chen, W. Zhang, J. Hu, Er-doped ZnO nanofibers for high sensibility detection of ethanol, Appl. Surf. Sci. 356 (2015) 73–80.

[5] K.C. Barick, S. Singh, M. Aslam, D. Bahadur, Porosity and photocatalytic studies of transition metal doped ZnO nanoclusters, Microporous Mesoporous Mater. 134 (2010) 195–202.

[6] R. Kumar, A. Umar, G. Kumar, M.S. Akhtar, Y. Wang, S.H. Kim, Ce-doped ZnO nanoparticles for efficient photocatalytic degradation of direct red-23 dye, Ceram. Int. 41 (2015) 7773–7782.

[7] W. Cai, P.R. de la Piscina, N. Homs, Oxidative steam reforming of bio-butanol for hydrogen production: effects of noble metals on bimetallic CoM/ZnO catalysts (M=Ru, Rh, Ir, Pd), Appl. Catal. B Environ. 145 (2014) 56–62.

[8] J.A. Torres, J. Llorca, A. Casanovas, M. Domínguez, J. Salvadó, D. Montané, Steam reforming of ethanol at moderate temperature: Multifactorial design analysis of Ni/$La_2O_3$-$Al_2O_3$, and Fe- and Mn-promoted Co/ZnO catalysts, J. Power Sources. 169 (2007) 158–166.

[9] H. Lei, R. Nie, G. Wu, Z. Hou, Hydrogenation of $CO_2$ to $CH_3OH$ over Cu/ZnO catalysts with different ZnO morphology, Fuel. 154 (2015) 161–166.

[10] B. Donkova, D. Dimitrov, M. Kostadinov, E. Mitkova, D. Mehandjiev, Catalytic and photocatalytic activity of lightly doped catalysts M : ZnO ( M = Cu , Mn ), Mater. Chem. Phys. 123 (2010) 563–568.

[11] J.-C. Chen, C.-T. Tang, Preparation and application of granular ZnO/$Al_2O_3$ catalyst for the removal of hazardous trichloroethylene., J. Hazard. Mater. 142 (2007) 88–96.

[12] M. Ashokkumar, S. Muthukumaran, Enhanced room temperature ferromagnetism and photoluminescence behavior of Cu-doped ZnO co-doped with Mn, Phys. E Low-Dimensional Syst. Nanostructures. 69 (2015) 354–359.

[13] R. Mimouni, O. Kamoun, A. Yumak, A. Mhamdi, K. Boubaker, P. Petkova, M. Amlouk, Effect of Mn content on structural, optical, opto-thermal and electrical properties of ZnO:Mn sprayed thin films compounds, J. Alloys Compd. 645 (2015) 100–111.

[14] M. Mazhdi, J. Saydi, M. Karimi, J. Seidi, F. Mazhdi, A study on optical, photoluminescence and thermoluminescence properties of ZnO and Mn doped-ZnO nanocrystalline particles, Opt. - Int. J. Light Electron Opt. 124 (2013) 4128–4133.

[15] V.M. De Almeida, A. Mesquita, A.O. De Zevallos, N.C. Mamani, P.P. Neves, X. Gratens, V.A. Chitta, W.B. Ferraz, A.C. Doriguetto, A.C Sabioni, H.B. De Carvalho, Room temperature ferromagnetism promoted by defects at zinc sites in Mn-doped ZnO, J. Alloys Compd. 655 (2016) 406–414.

[16] V.D. Mote, Y. Purushotham, B.N. Dole, Structural, morphological, physical and dielectric properties of Mn doped ZnO nanocrystals synthesized by sol–gel method, Mater. Des. 96 (2016) 99–105.

[17] F. Achouri, S. Corbel, L. Balan, K. Mozet, E. Girot, G. Medjahdi, M. Said, A. Ghrabi, R. Schneider, Porous Mn-doped ZnO nanoparticles for enhanced solar and visible light photocatalysis, Mater. Des. 101 (2016) 309–316.

[18] Q. Gao, Y. Dai, C. Li, L. Yang, X. Li, C. Cui, Correlation between oxygen vacancies and dopant concentration in Mn-doped ZnO nanoparticles synthesized by co-precipitation technique, J. Alloys Compd. 684 (2016) 669–676.

[19] S.K. Sharma, P.K. Pujari, K. Sudarshan, D. Dutta, M. Mahapatra, S. V. Godbole, O.D. Jayakumar, A.K. Tyagi, Positron annihilation studies in ZnO nanoparticles, Solid State Commun. 149 (2009) 550–554.

[20] L.C.Damonte, V.Donderis, M.A.Hernández fenollosa, Dopants incorporation in ZnO mechanical milled powders sensed by positrons, Hyp.Int. 179 (2007) 73-79.

[21] D. Wang, Z.Q. Chen, D.D. Wang, J. Gong, C.Y. Cao, Z. Tang, L. Huang, Effect of thermal annealing on the structure and magnetism of Fe-doped ZnO nanocrystals synthesized by solid state reaction, J. Magn. Magn. Mater. 322 (2010) 3642–3647.

[22] S. Chattopadhyay, S. Dutta, A. Banerjee, D. Jana, S. Bandyopadhyay, A. Sarkar, Synthesis and characterization of single-phase Mn-doped ZnO, Phys. B Condens. Matter. 404 (2009) 1509–1514.

[23] D. Sanyal, M. Chakrabarti, A. Chakrabarti, Synthesis and positron characterizations of ferromagnetic $Zn_{0.98}Mn_{0.02}O$ and paramagnetic $Zn_{0.98}Mn_{0.02}O$ samples, Solid State Commun. 150 (2010) 2266–2269.

[24] Q. Li, Y. Wang, J. Liu, W. Kong, B. Ye, Structural and magnetic properties in Mn-doped ZnO films prepared by pulsed-laser deposition, Appl. Surf. Sci. 289 (2014) 42–46.

[25] P. Kirkegaard, N.J. Pedersen, M.M. Eldrup, PATFIT-88: A Data-Processing System for Positron Annihilation Spectra on Mainframe and Personal Computers, 1989.

[26] J. Li, J. Chen, R. Ke, C. Luo, J. Hao, Effects of precursors on the surface Mn species and the activities for NO reduction over $MnO_x/TiO_2$ catalysts, Catal. Commun. 8 (2007) 1896–1900.

[27] M. Ahmad, E. Ahmed, W. Ahmed, A. Elhissi, Z.L. Hong, N.R. Khalid, Enhancing visible light responsive photocatalytic activity by decorating Mn-doped ZnO nanoparticles on graphene, Ceram. Int. 40 (2014) 10085–10097.

[28] D. Li, H. Haneda, Enhancement of photocatalytic activity of sprayed nitrogen-containing ZnO powders by coupling with metal oxides during the acetaldehyde decomposition., Chemosphere. 54 (2004) 1099–110.

[29] S. Bhattacharyya, A. Gedanken, A template-free, sonochemical route to porous ZnO nano-disks, Microporous Mesoporous Mater. 110 (2008) 553–559.

[30] X. Li, Z. Hu, J. Liu, D. Li, X. Zhang, J. Chen, J. Fang, Ga Doped ZnO Photonic Crystals with Enhanced Photocatalytic Activity and Its Reaction Mechanism, Applied Catal. B, Environ. 195 (2016) 29–38.

[31] S.S. Abdullahi, Y. Köseoğlu, S. Güner, S. Kazan, B. Kocaman, C.E. Ndikilar, Synthesis and characterization of Mn and Co codoped ZnO nanoparticles, Superlattices Microstruct. 83 (2015) 342–352.

[32] M. Peiteado, S. Sturm, A.C. Caballero, D. Makovec, $Mn_{3-x}Zn_xO_4$ spinel phases in the Zn–Mn–O system, Acta Mater. 56 (2008) 4028–4035.

[33] M. Peiteado, A.C. Caballero, D. Makovec, Diffusion and reactivity of ZnO–$MnO_x$ system, J. Solid State Chem. 180 (2007) 2459–2464.

[34] C. Jing, Y. Jiang, W. Bai, J. Chu, A. Liu, Synthesis of Mn-doped ZnO diluted magnetic semiconductors in the presence of ethyl acetoacetate under solvothermal conditions, J. Magn. Magn. Mater. 322 (2010) 2395–2400.

[35] S. Zhou, K. Potzger, G. Talut, J. von Borany, W. Skorupa, M. Helm, J. Fassbender, Using x-ray diffraction to identify precipitates in transition metal doped semiconductors, J. Appl. Phys. 103 (2008) 07D530.

[36] H.B. Ruan, L. Fang, D.C. Li, M. Saleem, G.P.. Qin, C.Y. Kong, Effect of dopant concentration on the structural, electrical and optical properties of Mn-doped ZnO films, Thin Solid Films. 519 (2011) 5078–5081.

[37] K. Ravichandran, K. Karthika, B. Sakthivel, N. Jabena Begum, S. Snega, K. Swaminathan, V.Senthamilselvi , Tuning the combined magnetic and antibacterial properties of ZnO nanopowders through Mn doping for biomedical applications, J. Magn. Magn. Mater. 358-359 (2014) 50–55.

[38] S. Husain, F. Rahman, W. Khan, H. Naqvi, Effects of Mn substitution on structural and optical properties of ZnO nanoparticles, in: AIP, 2013: pp. 33–34.

[39] Sharda, K. Jayanthi, S. Chawla, Synthesis of Mn doped ZnO nanoparticles with biocompatible capping, Appl. Surf. Sci. 256 (2010) 2630–2635.

[40] S.-J. Han, T.-H. Jang, Y.B. Kim, B.-G. Park, J.-H. Park, Y.H. Jeong, Magnetism in Mn-doped ZnO bulk samples prepared by solid state reaction, Appl. Phys. Lett. 83 (2003) 920.

[41] A. Tiwari, C. Jin, A. Kvit, D. Kumar, J.. Muth, J. Narayan, Structural, optical and magnetic properties of diluted magnetic semiconducting Zn1−xMnxO films, Solid State Commun. 121 (2002) 371–374.

[42] C. Cong, L. Liao, C. Li, L. Fan, K. Zhang, Synthesis, structure and ferromagnetic properties of Mn-doped ZnO nanoparticles, Nanotechnology. 16 (2005) 981–984.

[43] U. Ilyas, R.S. Rawat, G. Roshan, T.L. Tan, P. Lee, S.V. Springham, S. Zhang, L. Fengji, R. Chen, Quenching of surface traps in Mn doped ZnO thin films for enhanced optical transparency, Appl. Surf. Sci. 258 (2011) 890–897.

[44] W. Xiao, Q. Chen, Y. Wu, T. Wu, L. Dai, Ferromagnetism of $Zn_{0.95}Mn_{0.05}O$ controlled by concentration of zinc acetate in ionic liquid precursor, Mater. Chem. Phys. 123 (2010) 1–4.

[45] Y.Y. Tay, S. Li, C.Q. Sun, P. Chen, Size dependence of $Zn2p_{3/2}$ binding energy in nanocrystalline ZnO, Appl. Phys. Lett. 88 (2006) 173118.

[46] V.P. Santos, O.S. Soares, J.J.W. Bakker, M.F.R. Pereira, J.J.M. Órfão, J. Gascon, F. Kapteijn, J.L. Figueiredo, Structural and chemical disorder of cryptomelane promoted by alkali doping: Influence on catalytic properties, J. Catal. (2012).

[47] V.P. Santos, M.F.R. Pereira, J.J.M. Órfão, J.L. Figueiredo, The role of lattice oxygen on the activity of manganese oxides towards the oxidation of volatile organic compounds, Appl. Catal. B Environ. 99 (2010) 353–363.

[48] D. Hu, X. Liu, S. Deng, Y. Liu, Z. Feng, B. Han, Y. Wang, Y. Wang, Structural and optical properties of Mn-doped ZnO nanocrystalline thin films with the different dopant concentrations, Phys. E Low-Dimensional Syst. Nanostructures. 61 (2014) 14–22.

[49] C.-J. Li, G.-R. Xu, Zn–Mn–O heterostructures: Study on preparation, magnetic and photocatalytic properties, Mater. Sci. Eng. B. 176 (2011) 552–558.

[50] L. Duan, X. Zhao, J. Liu, W. Geng, H. Xie, S. Chen, Structural, thermal and magnetic investigations of heavily Mn-doped ZnO nanoparticles, J. Magn. Magn. Mater. 323 (2011) 2374–2379.

[51] R.K. Singhal, M.S. Dhawan, S.K. Gaur, S.N. Dolia, S. Kumar, T. Shripathi, U. Deshpande, Y. Xing, E. Saitovitch, K. B. Garg, , Room temperature ferromagnetism in Mn-doped dilute ZnO semiconductor: An electronic structure study using X-ray photoemission, J. Alloys Compd. 477 (2009) 379–385.

[52] H. Zhang, B. Chen, H. Jiang, C. Wang, H. Wang, X. Wang, A strategy for ZnO nanorod mediated multi-mode cancer treatment, Biomaterials. 32 (2011) 1906–1914.

[53] N.M. Hosny, A. Dahshan, Facile synthesis and optical band gap calculation of $Mn_3O_4$ nanoparticles, Mater. Chem. Phys. 137 (2012) 637–643.

[54] R. Krause-Rehberg, H.S. Leipner, T. Abgarjan, A. Polity, Review of defect investigations by means of positron annihilation in II-VI compound semiconductors, Appl. Phys. A. 66 (1998) 599–614.

[55] P. Hautojärvi, C. Corbel, Positron Spectroscopy of Defects in Metals and Semiconductors, in: A. Dupasquier, A.P. Millis (Eds.), Positron Spectrosc. Solids, Amsterdam, 1995: pp. 491 – 532.

[56] L.C. Damonte, L.A. Mendoza Zélis, B. Marí Soucase, M.A. Hernández Fenollosa, Nanoparticles of ZnO obtained by mechanical milling, Powder Technol. 148 (2004) 15–19.

[57] S.K. Neogi, R. Karmakar, A.K. Misra, A. Banerjee, D. Das, S. Bandyopadhyay, Physical properties of antiferromagnetic Mn doped ZnO samples: Role of impurity phase, J. Magn. Magn. Mater. 346 (2013) 130–137.

[58] T. Ghoshal, S. Kar, S. Biswas, S.K. De, P. Nambissan, Vacancy-type defects and their evolution under Mn substitution in single crystalline ZnO nanocones studied by positron annihilation, J. Phys. Chem. C. 113 (2009) 3419–3425.

# Tables

**Table 1.** Nomenclature, composition and Egap values for direct transitions of the Mn-doped ZnO solids ( * Atomic Absorption Spectroscopy)

| Sample | Nominal Mn (wt%) | Observed Mn (wt%)* | $S_{BET}$ ($m^2$ $g^{-1}$) | Egap (eV) |
|---|---|---|---|---|
| ZnO | 0 | 0 | 3 | 3,18 |
| 5MnZnO | 5 | 3 | 4 | 3,19 |
| 10MnZnO | 10 | 9 | 6 | 3,20 |
| 15MnZnO | 15 | 12 | 9 | 3,6 |
| 20MnZnO | 20 | 17 | 11 | 3,7 |
| $Mn_2O_3$ | | | | 3,69 [52] |
| $Mn_3O_4$ | | | | 3,75 [52] |

**Table 2.** . XRD peak position and crystallite size of Mn-doped ZnO samples.

| Sample | Peak position, 2θ ($^o$) | Average crystallite size, D (nm) | Strain (%) | d-Value (*Å*) | *Cell parameters (Å)* | | |
|---|---|---|---|---|---|---|---|
| | | | | | *a=b* | *c* | *c/a* |
| ZnO | 36.32 | 51.39 | 0.23 | 2.4713 | 3.2427 | 5.2033 | 1.605 |
| 5MnZnO | 36.28 | 52.31 | 0.22 | 2.4745 | 3.2467 | 5.2107 | 1.605 |
| 10MnZnO | 36.28 | 51.38 | 0.23 | 2.4745 | 3.2474 | 5.2068 | 1.603 |
| 15MnZnO | 36.26 | 51.38 | 0.23 | 2.4753 | 3.2509 | 5.1947 | 1.598 |
| 20MnZnO | 36.31 | 46.22 | 0.25 | 2.4721 | 3.2450 | 5.1976 | 1.602 |

**Table 3.** XPS results of the Mn-doped ZnO solids.

| Sample | Zn 2p | O 1s | | $Mn2p_{3/2}$ | |
|---|---|---|---|---|---|
| ZnO | 1021.6 | 530.3 (40) | 532.2 (60) | | |
| 5MnZnO | 1021.3 | 530.5 (87) | 532.5 (13) | 640.5 (76) | 643.4 (24) |
| 10MnZnO | 1021.4 | 531.1 (78) | 532.5 (22) | 640.8 (75) | 643.6 (25) |
| 15MnZnO | 1021.0 | 529.3 (18) | 531.2 (82) | 640.9 (68) | 642.6 (32) |
| 20MnZnO | 1020.9 | 529.1 (17) | 531.0 (83) | 640.7 (65) | 642.5 (35) |

# Figure Captions.

Figure 1. X-ray diffraction patterns of samples: (a) ZnO; (b) 5MnZnO; (c) 10MnZnO; (d) 15MnZnO and (e) 20MnZnO.

Figure 2. Images of samples: (a) SEM image of ZnO; sample 10MnZnO: (b) SEM image of 10MnZnO; (c) TEM image of 10MnZnO; (d) Zn mapping and (e) Mn mapping of 10MnZnO.

Figure 3. XPS spectra of the(a) ZnO; (b) 5MnZnO; (c)10MnZnO; (d) 15MnZnO and (e) 20MnZnO in the Zn 2p core level region.

Figure 4. XPS spectra of the (a)ZnO; (b)5MnZnO; (c)10MnZnO; (d) 15MnZnO and (e) 20Mn-ZnO in the O 1s core level region.

Figure 5. XPS spectra of the (a) 5MnZnO; (b)10MnZnO; (c) 15MnZnO and (d) 20Mn-ZnO in the Mn 2p core level region.

Figure 6. Plot $(\alpha E_f)^2$ vs $E_f$ of Mn-ZnO samples. (a) ZnO; (b) 5MnZnO; (c)10MnZnO; (d) 15MnZnO and (e) 20MnZnO

Figure 7. Positron annihilation parameters evolution with Mn content.

**Figure 1.**

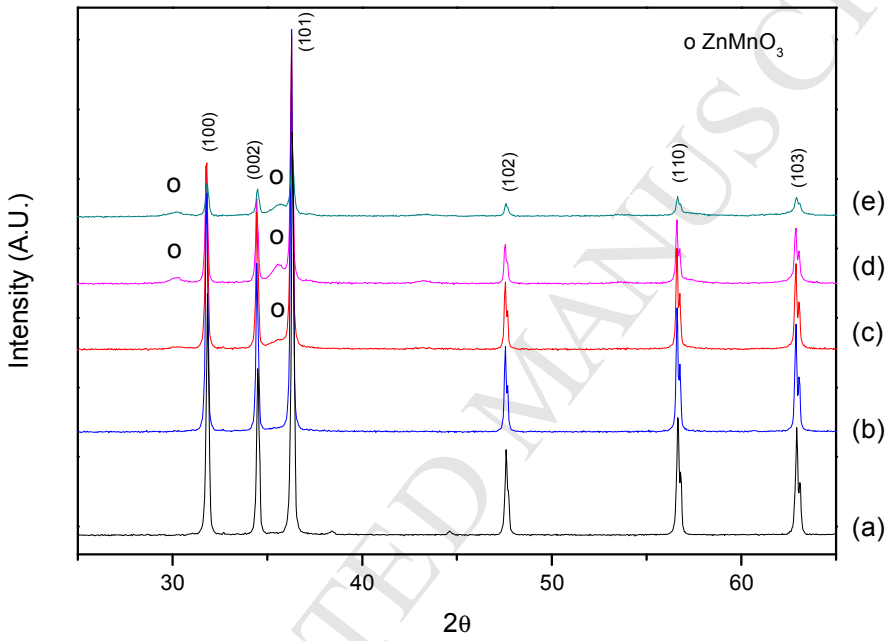

**Figure 2.**

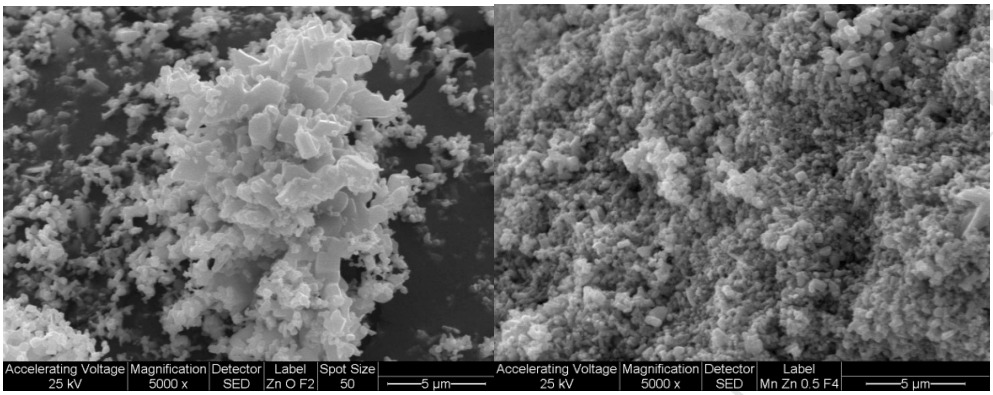


(a) (b)

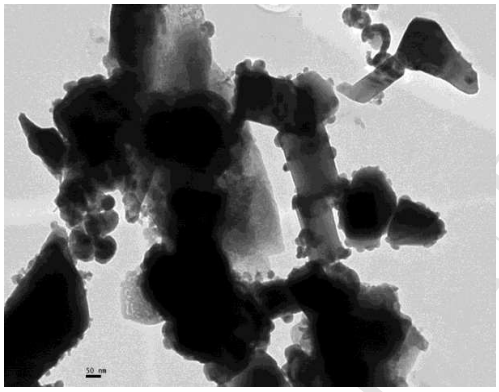

(c)

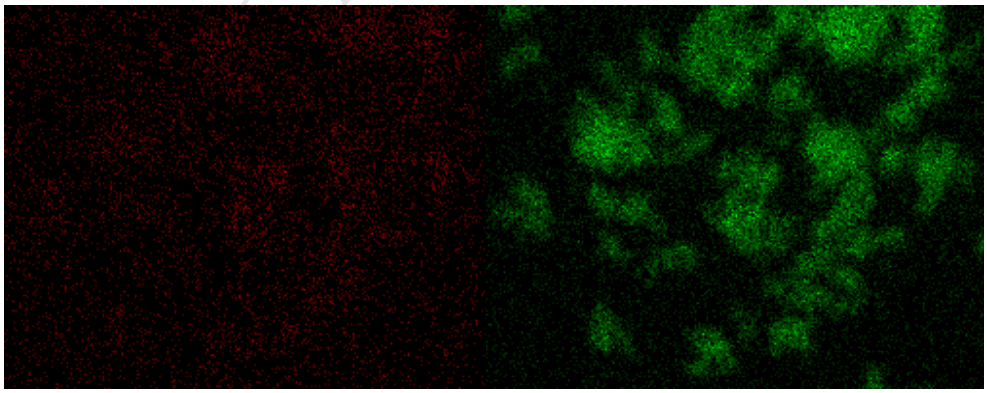

(d) (e)

**Figure 3.**

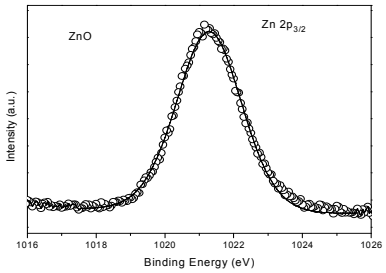


(a)

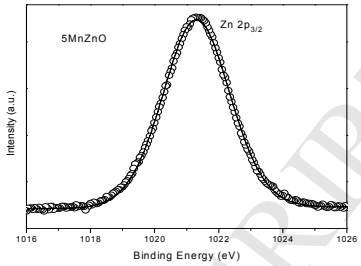


(b)

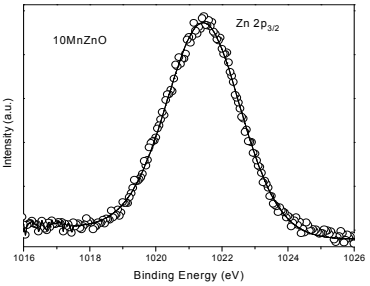


(c)

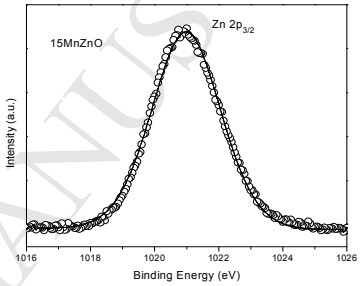


(d)

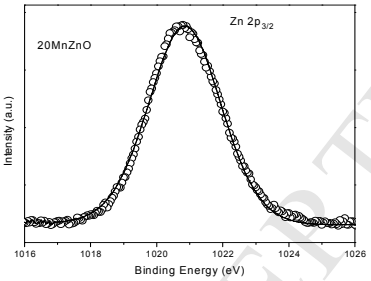


(e)

**Figure 4.**

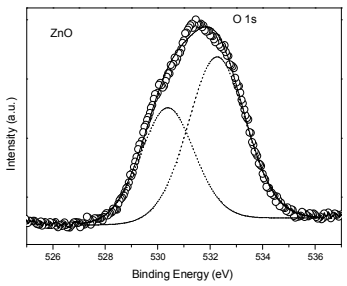


(a)

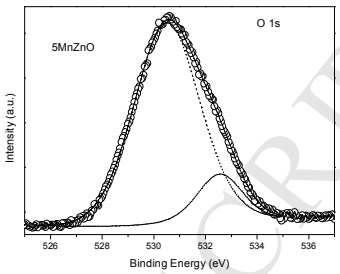


(b)

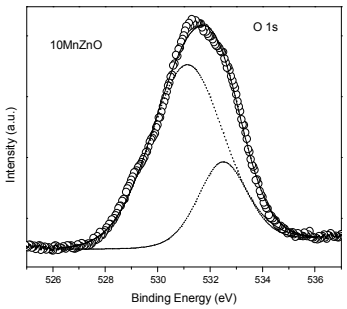


(c)

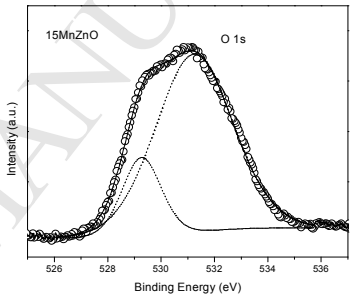


(d)

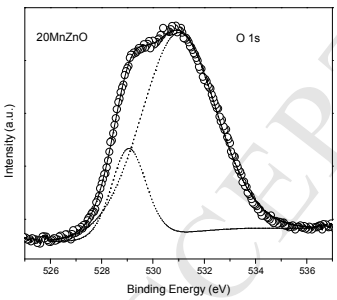


(e)

**Figure 5.**

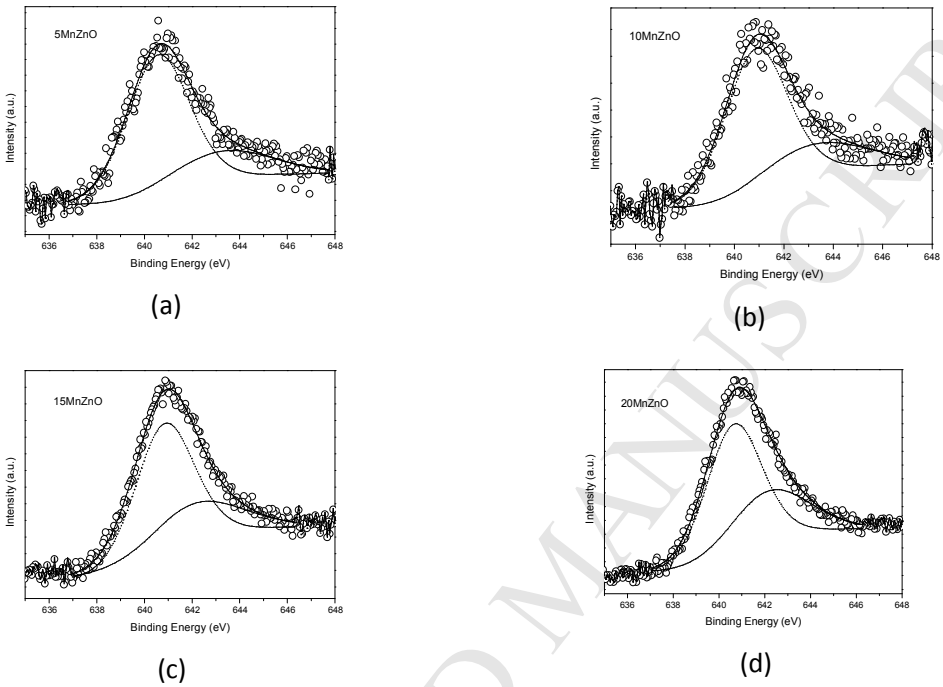

**Figure 6.**

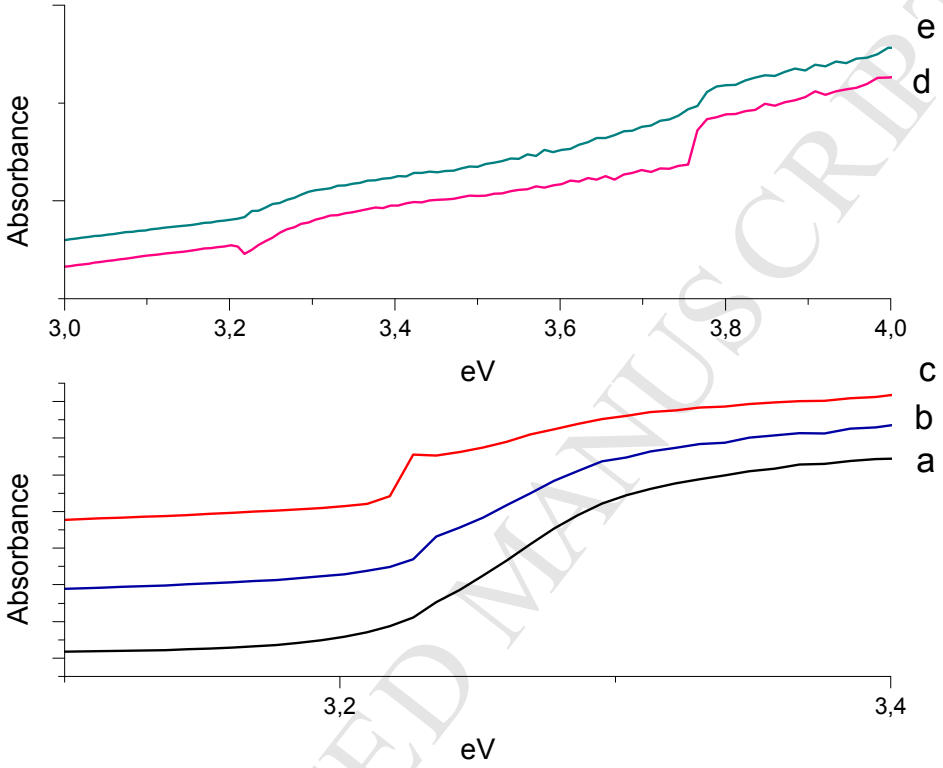

**Figure7.**

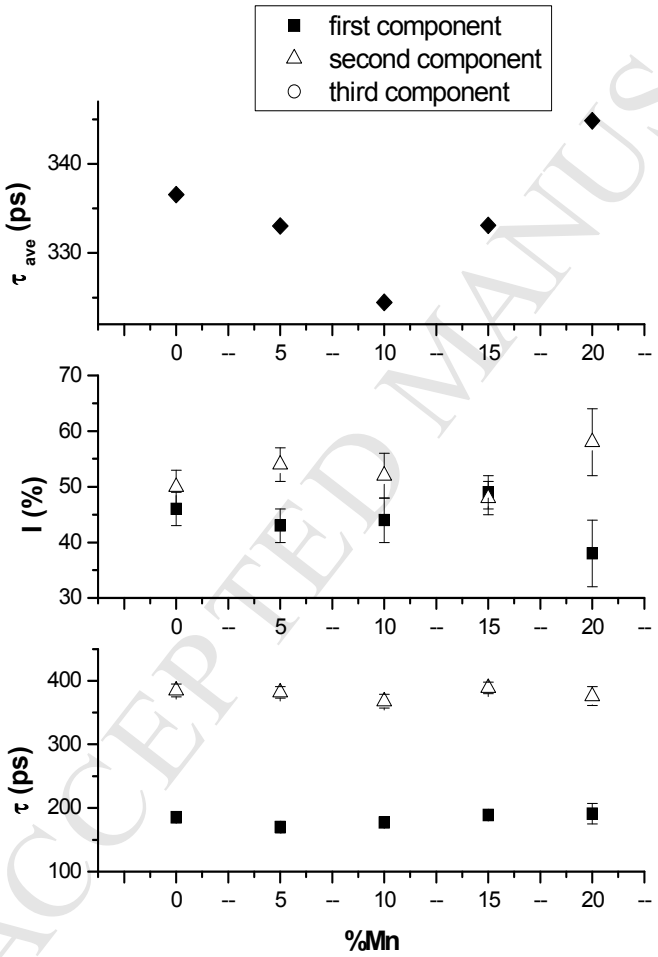

Highlights for "*Structural and optical properties of ZnO and Manganese-doped ZnO"*

Mn oxides supported on ZnO were prepared by impregnation with manganese nitrate.

$Mn^{4+}$ concentration increases with increasing the manganese content.

Segregation of $ZnMnO_3$ phase is observed for high Mn concentration.

Above manganese solubility limit too many oxygen defects in the oxide are formed.

Average positron annihilation lifetime evolution accompanies defect generation.